RESEARCH ARTICLE

JOR *Spine* OPEN ACCESS

An additively manufactured model for preclinical testing of cervical devices

Jenna M. Wahbeh [1,2] ⬤ | Erika Hookasian [1,2] | John Lama [1,2] | Labiba Alam [1,2] | Sang-Hyun Park [1,3] | Sophia N. Sangiorgio [1,2,3] | Edward Ebramzadeh [1,3]

[1]The J. Vernon Luck, Sr., M.D. Orthopaedic Research Center, Luskin Orthopaedic Institute for Children, Los Angeles, California, USA

[2]Department of Bioengineering, UCLA, Los Angeles, California, USA

[3]Department of Orthopaedic Surgery, UCLA, Los Angeles, California, USA

Correspondence
Edward Ebramzadeh, JVL Orthopaedic Research Center, Luskin Orthopaedic Institute for Children, 403 West Adams Boulevard, Los Angeles, CA 90007, USA.
Email: eebramzadeh@mednet.ucla.edu

Abstract

Purpose: Composite models have become commonplace for the assessment of fixation and stability of total joint replacements; however, there are no comparable models for the cervical spine to evaluate fixation. The goal of this study was to create the framework for a tunable non-homogeneous model of cervical vertebral body by identifying the relationships between strength, in-fill density, and lattice structure and creating a final architectural framework for specific strengths to be applied to the model.

Methods: The range of material properties for cervical spine were identified from literature. Using additive manufacturing software, rectangular prints with three lattice structures, gyroid, triangle, zig-zag, and a range of in-fill densities were 3D-printed. The compressive and shear strengths for all combinations were calculated in the axial and coronal planes. Eleven unique vertebral regions were selected to represent the distribution of density. Each bone density was converted to strength and subsequently correlated to the lattice structure and in-fill density with the desired material properties. Finally, a complete cervical vertebra model was 3D-printed to ensure sufficient print quality.

Results: Materials testing identified a relationship between in-fill densities and strength for all lattice structures. The axial compressive strength of the gyroid specimens ranged from 1.5 MPa at 10% infill to 31.3 MPa at 100% infill and the triangle structure ranged from 2.7 MPa at 10% infill to 58.4 MPa at 100% infill. Based on these results, a cervical vertebra model was created utilizing cervical cancellous strength values and the corresponding in-fill density and lattice structure combination. This model was then printed with 11 different in-fill densities ranging from 33% gyroid to 84% triangle to ensure successful integration of the non-homogeneous in-fill densities and lattice structures.

Conclusions: The findings from this study introduced a framework for using additive manufacturing to create a tunable, customizable biomimetic model of a cervical vertebra.

KEYWORDS
biomechanical testing, cervical disc replacement, cervical spine, composite model, preclinical model

1 | INTRODUCTION

Cervical disc replacements (CDRs) were designed with the intention to restore natural kinematics to patients that would typically undergo fusion surgery.[1–5] This patient population is relatively young, with an average age of 45.2 ± 5.2 years at the time of surgery, indicating that ideally, these devices should survive beyond 30 years.[6,7] While numerous CDR designs have been introduced over the past two decades, the majority have since been withdrawn from the market due to a failure to meet clinical expectation, with high complication rates such as adjacent segment degeneration, heterotopic ossification, and mechanical failures associated with potential revision surgeries.[8–11] Specifically, many devices have migrated within the vertebral bodies or loosened. In clinical studies with a minimum of 2 years of follow-up, migration and loosening rates of 2%–17% have been reported, typically resulting in a subsequent surgery.[9,12–18] Furthermore, the Food and Drug Administration website for Manufacturer and User Facility Device Experience (MAUDE) indicates that 25% of devices failing at 5-years are due to mechanical complications such as migration, loosening, and subsidence.[11] While numerous studies have evaluated the kinematics of the cervical spine following CDRs, to our knowledge, no biomechanical studies have evaluated the fixation of CDRs within the vertebra in a composite or cadaveric model.[19–24]

Fixation testing of total hip and knee replacements using composite model bones have been conducted for more than three decades by investigators world-wide.[25–31] These biomimetic models utilize reinforced epoxy resin to simulate cortical bone and rigid polyurethane foam to replicate cancellous bone, resulting in a highly reproducible model that can withstand extensive cyclic loading without decay, as well as higher loads than typical cadaver specimens.[32–35] Through this in vitro testing, invaluable knowledge of implant performance has contributed to the development and understanding of fixation features and surface modifications that enhance long-term fixation and stability. This has resulted in decreased revisions due to loosening and migration for joint replacements.[25,26,36,37] The striking lack of biomechanical studies to assess fixation of CDRs may be due to the fact that there are no standardized models or methods available to conduct such studies. To address this gap, the availability of a biofidelic, reproducible cervical vertebral body model may be useful.

Additive manufacturing (AM) techniques may provide a tangible solution for producing replicable, cost-effective spinal models for biomechanical testing. Specifically, three-dimensional (3D) printing techniques have been widely adopted for surgical preparation, to create patient specific models, or customized implants.[38,39] These techniques have also been used to create anatomical models for preoperative and intraoperative planning and reference and for resident education.[32,40,41] Natural cellular structures have been widely studied for their material properties and the relationship of the specific features in these structures to strengths.[42,43] These cellular structures and relationships have been used to inform the creation of additively manufactured lattice structures, such as a honeycomb or gyroid structure.[44] Based on these previous findings, these lattice structures can now be leveraged for specific applications. One such application that has not been widely investigated is the use of 3D printing for the creation of synthetic vertebral models for the purpose of biomechanical testing of disc replacements. Therefore, the goal of this study was to create the framework for a tunable non-homogeneous model of a cervical vertebral body by identifying the relationships between strength, in-fill density, and lattice structure to create a final architectural framework for specific strengths to be applied to the model.

2 | METHODS

A comprehensive literature search was performed to identify an acceptable range of shear and compressive strength values for the expected range of cancellous bone in the cervical spine. Two studies reported compressive strength specifically in the cervical spine (Table 1).[45–50] However, no articles were found that identified the modulus of elasticity or shear strength of cancellous bone in the cervical spine. Therefore, lumbar spine properties were used as a close alternative. Specifically, one study assessed the shear strength of the lumbar spine, and three studies assessed modulus of elasticity in the lumbar spine (Table 1). These values were utilized to determine if the lattice structures and in-fill densities were feasible as a cadaveric specimen replacement.

2.1 | Strength calculations

Following a comprehensive literature review, a previous study was identified that defined 11 unique regions for the cervical vertebra, based on differences in bone density assessed from CT images.[51] Therefore, original calculations were made to determine the strength at specific locations in the spine, as bone properties vary by vertebral location. Two equations that related cervical compressive strength (*cs*) and bone mineral density (*d*) were given in Lang et al.[52] and McBroom et al.[53] The specific equations were chosen since their specificity to vertebral bodies was advantageous in this study, compared to previous equations that related compressive strength and bone mineral density.[54] However, these equations follow similar principles from the widely accepted equations from Carter and Hayes.[55] The following equations were used to calculate the compressive strength at the 11 anatomical locations specified.[51] These values were referenced for validation of best fit models and creation of the final vertebral body model (Figure 1).

Lang et al. $cs = 8.2 \times 10^{-6} \times d^{2.45} + 0.082.$

McBroom et al. $cs = 17.4 \times 10^{-6} \times 0.01 d^{2.26}.$

2.2 | Print design

For the measurement of yield compressive and shear strength, specimens were printed according to ASTM Standard D659 and D5729-21 using Ultimaker Cura software (UltiMaker, Zaltbommel, NL).

TABLE 1 Material strength properties used in this study.

Property measured	Taken from: Author, year	Part of spine	Reported value
Cancellous compressive strength	Feng et al., 2021	Cervical	6 MPa
	Shim et al., 2005	Cervical	5.1 MPa
Cancellous shear strength	Xavier et al., 2017	Lumbar	0.5–1.5 MPa
Modulus of elasticity	Nicholson et al., 1997	Lumbar	165 MPa, 43 MPa
	Ogurkowska and Błaszczyk, 2020	Lumbar	32.8–41.5 MPa
	Wang et al., 2022	Lumbar	61.7 ± 15.9 MPa
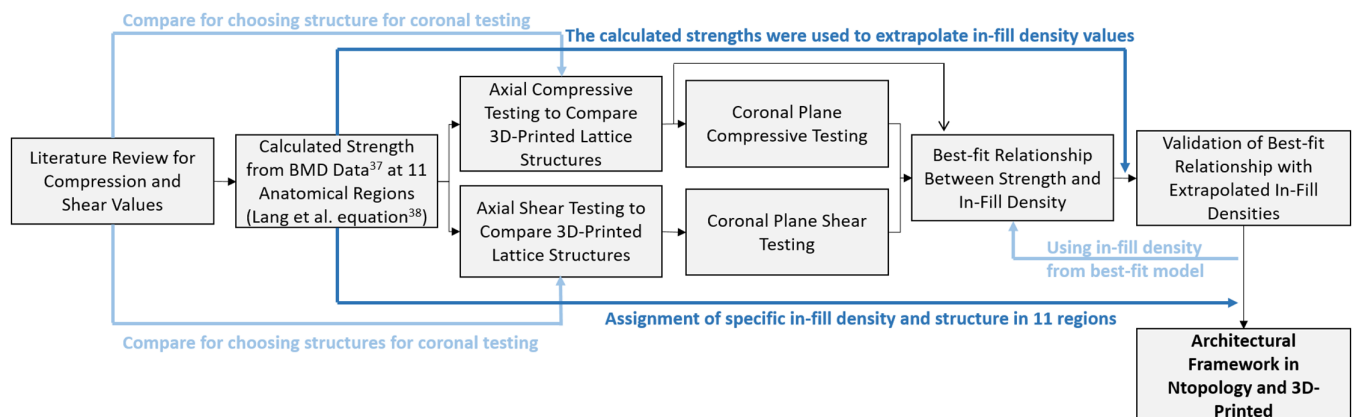
FIGURE 1 Flow chart depicting the steps where values identified in literature were referenced and the original calculations from bone mineral densities (BMD) identified by Anderst et al.[51] and calculated with the equations from Lang et al.[52] were referenced for the final selection of in-fill density and lattice structure of a cervical vertebral body model.

Specifically, rectangular specimens of 12.7 × 12.7 × 25.4 mm were printed on an Ultimaker S5 Pro printer in varying in-fill densities and lattice structures (UltiMaker, Zaltbommel, NL). Three lattice structures were selected for evaluation—triangle, zig zag, and gyroid (Figure 2). All specimens were made from poly lactic acid (PLA) with in-fill densities ranging from 5% to 35%, increasing in increments of 5%. Following this, in-fill densities of 60% and 100% were printed for all lattice structures, as well.

The in-fill density refers to the amount of print material throughout the rectangular prints, for example, 5% means the inside of the rectangular print will only be 5% filled and 95% will be empty space between layers and between the lattice structure. Although 100% in-fill density implies the entire print will be the material, the results may vary from structure to structure as the material is still printed with the specific in-fill density and this may affect the overall strength.

In accordance with ASTM Standard D695, $N = 5$ specimens were tested with each in-fill density and lattice structure sample group, for a total of $N = 105$ specimens in each testing setup. Upon completion of successful prints, each combination of variables was tested in compression and shear testing until failure to assess material strength. One lattice structure was chosen to be further tested for anisotropic properties, based on similarities to cancellous bone. Specifically, failure patterns and the relationship between strength and in-fill density were evaluated to determine the most similar structure. Anisotropic properties were tested by orienting the specimens at two different orientations, perpendicular to each other. This ensured that the in-fill density was being evaluated for transverse and axial properties, parallel and perpendicular to the print orientation.

2.3 | Compression testing

Specimens were tested in compression using a biaxial servo-hydraulic load frame (858 Mini Bionix; MTS Systems, Eden Prairie, MN). Axial load was applied through a ball-and-socket joint to ensure pure compression was applied uniformly across the top surface of the specimens (Figure 3). Following ASTM Standard D695-15, specimens were tested at a rate of 1.3 ± 0.3 mm/min and the load was recorded until they failed. Failure was defined as the formation of any mechanical defect such as buckling or cracking during testing.

2.4 | Shear testing

Custom plates were designed for shear testing to securely insert the prints at both the top and bottom faces of the specimens (Figure 4). Plates were then secured to the ball-and-socket joint to apply torsional load. Following ASTM Standard D5729-21, specimens were tested in torsion at a frequency of 0.01 Hz, or 3.6°/s, until the specimens failed. Failure was defined as the formation of any mechanical defect such as buckling or cracking during testing.
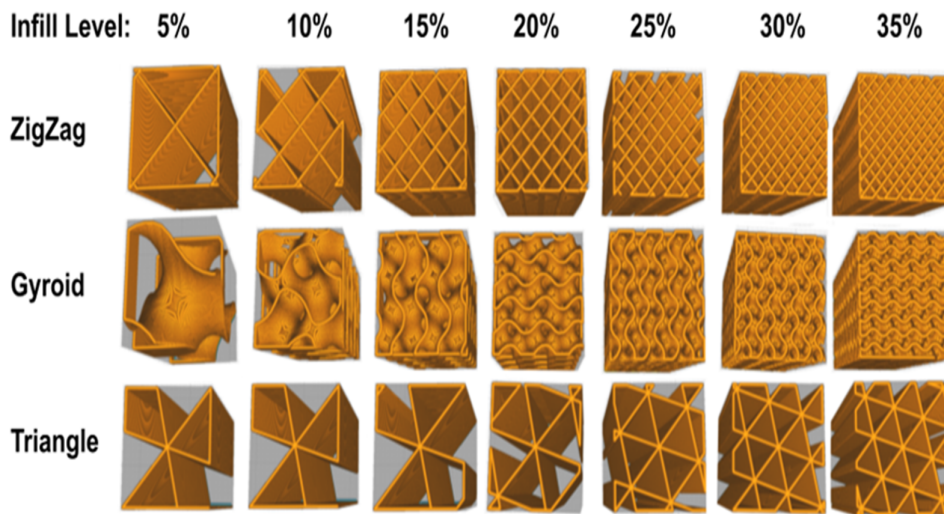
FIGURE 2 Three lattice structures and initial print densities. In addition to the matrix above, in-fill densities of 60% and 100% were tested for each of the three lattice structures.
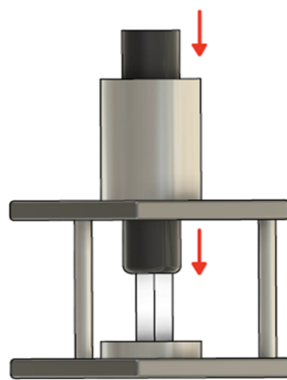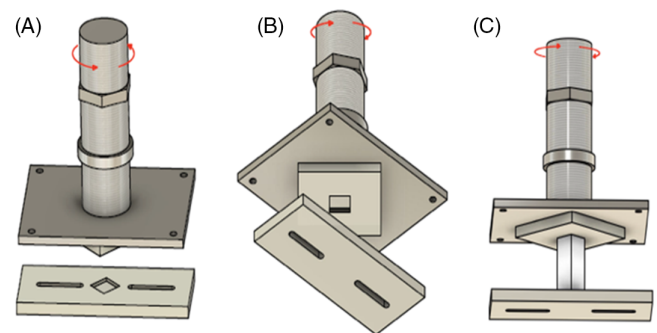

FIGURE 3 Custom compressive testing apparatus.

FIGURE 4 Custom shear testing apparatus.

2.5 | Strength relationships

A best-fit relationship was then calculated for each lattice structure and density. The best-fit model was validated through testing of in-fill densities that were chosen over 35% in both compression and shear. Specifically, the strengths calculated from Lang et al. at the 11 distinct regions of the cervical spine were used to extrapolate a specific in-fill density that would be required to achieve that. Those in-fill densities were then printed and tested for further validation of the relationships created following the same compression testing protocol to ensure accuracy among the extrapolated values and the actual mechanical properties of the chosen structures.

2.6 | Model creation

Following this, a custom 3D part was developed in nTopology with separate regions for each anatomical location. This computer model created the architectural framework for the customizable model. In-fill densities and lattice structures were assigned to each section to match the previously calculated strength values at those regions in this study.[51] This model was then exported into the Ultimaker

software. Finally, the 3D-printed model was printed to ensure a seamless integration of the custom in-fill densities and lattice structures and sufficient print quality.

2.7 | Data reduction

A stress versus strain plot was created for every specimen by calculating the stress and strain at each time point, the linear portion was manually defined, and the modulus of elasticity was calculated from this slope. A custom MATLAB program (version: R2020a; Mathworks, Natick, MA) was utilized to calculate the compressive strength, shear strength, and modulus of elasticity. Compressive strength was determined by dividing the compressive yield load by the cross-sectional area. Shear strength was determined by the following equation where "T" is torque at failure, "c" is the distance from the center, and J is the polar moment of inertia:

$$\tau = \frac{Tc}{J}$$

Means and standard deviations were calculated for each group and compared using analysis of variance (ANOVA). Specifically, the

TABLE 2 Regions of cervical cancellous bone, respective density, and strength calculations.

Region	Density (mg/cc)	Strength (MPa) via Lang et al.	Strength (MPa) via McBroom et al.
Pedicle	630	59.3	61.2
Lamina	555	43.5	46.0
Lateral mass	550	42.5	45.1
Exterior body	455	26.8	29.4
Spinous process	430	23.3	25.8
Exterior body (posterior)	415	21.4	23.8
Uncinate process	410	20.7	23.2
Exterior body (anterior)	370	16.2	18.4
Central body (lateral)	355	14.6	16.8
Central body (posterior)	350	14.1	16.2
Central body (anterior)	295	9.3	11.0

strength was compared between each lattice structure at the tested in-fill densities. All statistical tests were performed using SPSS Version 19.0 (IBM, Inc., Houston, TX). If a significant difference was detected between the lattice structures with a $p < 0.05$, the p-value was reported. Additionally, a power analysis was conducted to determine if a sample size of 5, recommended by ASTM, would be sufficient in the present experiment. The main outcome of interest for the power analysis was considered the strength of each sample type. Given an alpha level of 0.05 and a desired power of 80%, and a standard deviation of 0.5 MPa, the experiments were able to detect differences in strength between different lattice structures of 1 MPa or greater. This was considered sufficient power since the standard deviations were generally below 0.5 MPa.

3 | RESULTS

3.1 | Strength calculations

Utilizing the equations by Lang et al. and McBroom et al., strength was calculated at 11 anatomical locations in the cervical spine using the bone mineral densities obtained through literature. Both equations provided similar results for cervical cancellous bone strength (Table 2). Therefore, the strengths from Lang et al. were chosen to be compared to the strengths calculated from each in-fill density for assignment to the specific regions.

3.2 | Compression testing

A total of 100 3D-printed specimens of known dimension were tested successfully under axial compressive loading. The zig-zag specimens had axial compressive strengths of 0.4 ± 0.1 MPa for 5% in-fill, 1.3 ± 0.1 MPa for 10% in-fill, 3.1 ± 0.3MP for 15% in-fill, 3.0 ± 0.3 MPa for 20% in-fill, 9.3 ± 0.4 MPa for 25% in-fill, 10.4 ± 0.8 MPa for 30% in-fill, 14.1 ± 0.3 MPa for 35% in-fill, 27.2 ± 0.5 MPa for 60% in-fill, and 55.5 ± 3.2 MPa for 100% in-fill (Figure 5). The gyroid specimens
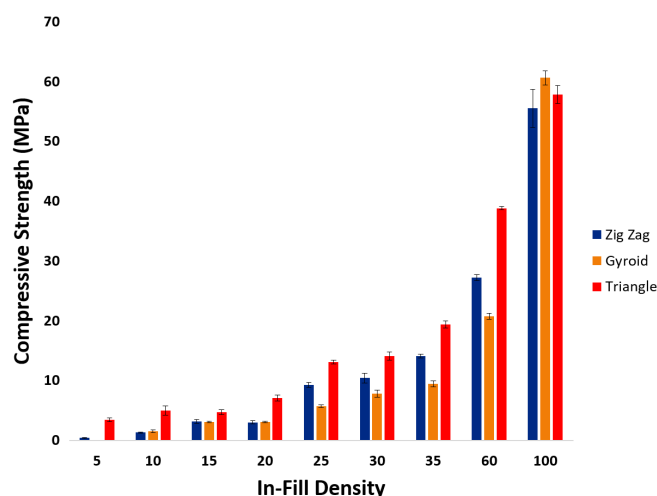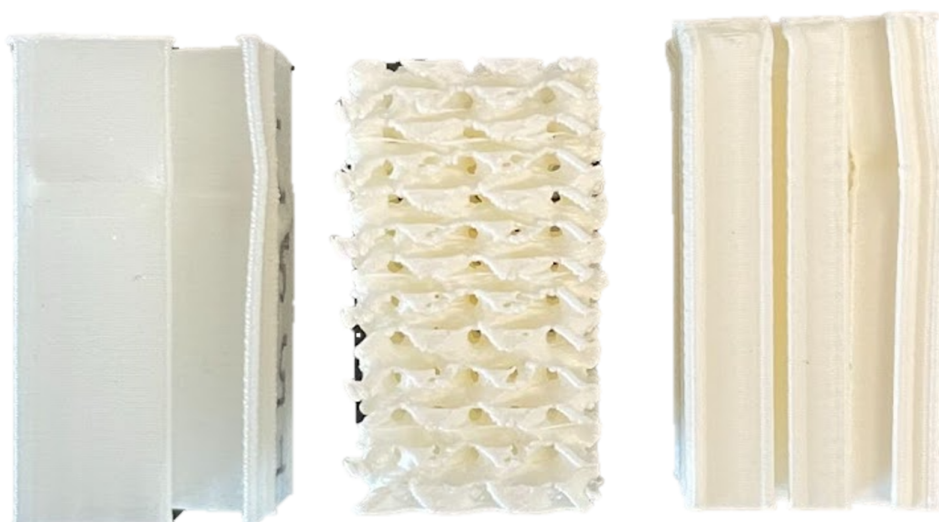

FIGURE 5 Calculated compressive strength for each in-fill density and specific lattice structure, calculated based on the ultimate force at failure and the cross-sectional area of each specimen. Each lattice structure was significantly different at the specific in-fill densities ($p < 0.01$).

with 5% in-fill densities could not be tested as the print density was too low to form specimens capable of withstanding testing. However, the gyroid specimens had axial compressive values of 1.5 ± 0.2 MPa for 10% in-fill, 3.1 ± 0.1 MPa for 15% in-fill, 3.1 ± 0.1 MPa for 20% in-fill, 5.7 ± 0.2 MPa for 25% in-fill, 7.8 ± 0.6 MPa for 30% in-fill, 9.5 ± 0.5 MPa for 35% in-fill, 20.7 ± 0.5 MPa for 60% in-fill, and 60.6 ± 1.2 MPa for 100% in-fill (Figure 5). Finally, triangle specimens had axial strengths of 3.4 ± 0.3 MPa for 5% in-fill, 4.9 ± 0.8 MPa for 10% in-fill, 4.7 ± 0.4 MPa for 15% in-fill, 7.0 ± 0.5 MPa for 20% in-fill, 13.1 ± 0.3 MPa for 25% in-fill, 14.1 ± 0.7 MPa for 30% in-fill, 19.4 ± 0.6 MPa for 35% in-fill, 38.8 ± 0.3 MPa for 60% in-fill, and 57.8 ± 1.5 MPa for 100% in-fill (Figure 5). Statistical differences were found between all three lattice structures at each in-fill density following ANOVA testing ($p < 0.01$).

Failure modes were recorded for each specimen. All gyroid specimens were crushed following compression loading, with a visible loss

FIGURE 6 Compressive failures of the different lattice structures, from left, zig-zag, gyroid, triangle, showing buckling of the zig-zag and triangle and visible loss of height in the gyroid.
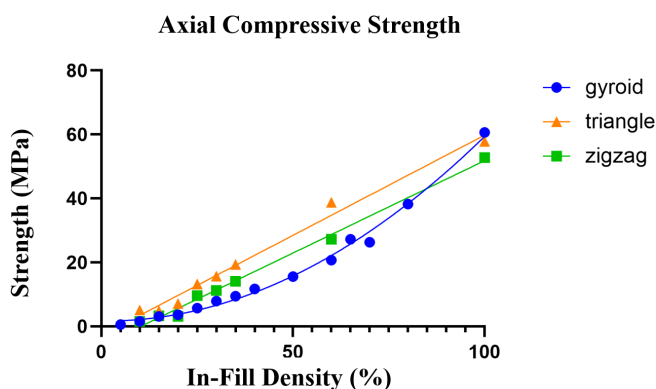
FIGURE 7 Measured axial compressive strength for each lattice structure with best-fit model for each. The curvilinear line fit best for the calculated gyroid strengths and was therefore used to better model this relationship between the strength and in-fill density for this lattice structure.

in height. Both zig-zag and triangle specimens buckled in the center of the specimen (Figure 6).

From the calculated strengths, a representative model was created for each lattice structure, relating the in-fill density to the compressive strength (Figure 7). For both triangle and zig-zag, a linear model was best fit, whereas an exponential model was best-fit for the gyroid structures. The following equations were extracted for gyroid, zig-zag, and triangle, where x is the in-fill density:

Gyroid: Strength $= 0.001x^2 + 0.01x - 1.7$.

Triangle: Strength $= 0.63x - 2.9$.

Zig-zag: Strength $= 0.58x - 5.9$.

Following axial testing, gyroid specimens were identified as the most structurally similar to cancellous bone. Specifically, these were chosen to be further tested as the range of cancellous bone compressive strength in the cervical spine varies between 5.1 and 6 MPa and the gyroid specimens had a low enough compressive strength to accommodate these values.[49,50] Furthermore, the final relationship
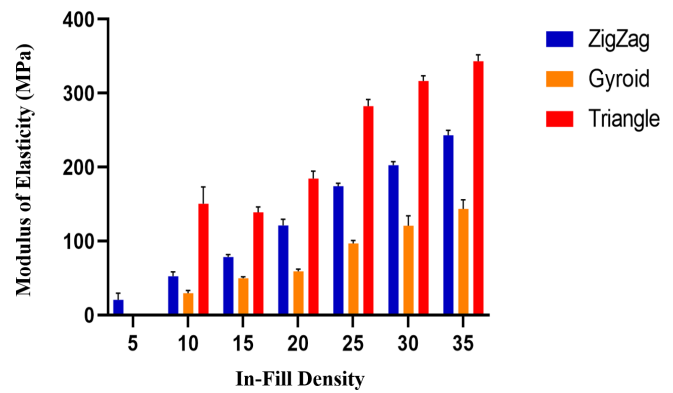
between the density and strength had a relationship more similar to that of cancellous bone, specifically this was an exponential relationship compared to the triangle and zig-zag, which were linear. Finally, failure patterns were analyzed, and it was noted that while the zig-zag and triangle lattice structures buckled at failure, the gyroid was the only structure to be crushed, with a visible loss in height. This failure mode is most similar to that of cancellous bone, as well, with the cancellous bone pores fracturing, resulting in crushing of the whole specimen.[56] Therefore, gyroid specimens were tested in coronal plane compression from 10% to 35% in-fill densities. The coronal compressive strengths were 0.2 ± 0.1 MPa for 10% in-fill, 1.4 ± 0.1 MPa for 15% in-fill, 3.7 ± 0.2 MPa for 20% in-fill, 4.4 ± 0.2 MPa 25% in-fill, 5.9 ± 0.1 MPa 30% in-fill, and 7.8 ± 0.4 MPa for 35% in-fill (Figure 8).
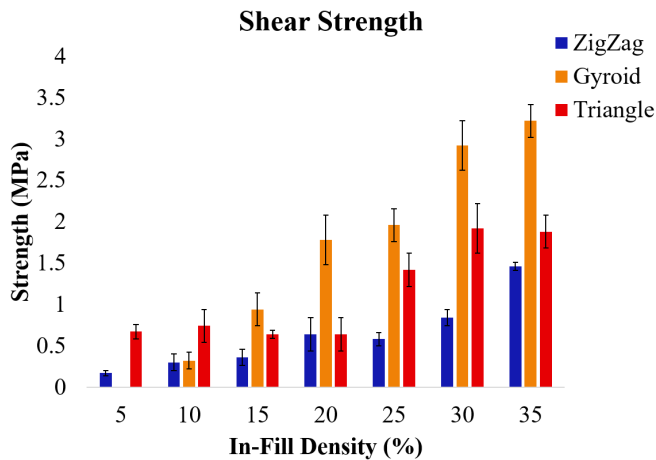
3.3 | Shear testing

A new set of five specimens for each of the three lattice structures were tested from 5% to 35% for each lattice structure in axial shear. Accordingly, the zig-zag specimens had an axial shear strength of 0.17 ± 0.09 MPa for 5% in-fill, 0.31 ± 0.1 MPa for 10% in-fill, 0.35 ± 0.1 MPa for 15% in-fill, 0.64 ± 0.2 MPa for 20% in-fill, 0.58 ± 0.08 MPa for 25% in-fill, 0.86 ± 0.1 MPa for 30% in-fill, and 1.44 ± 0.05 MPa for 35% in-fill. Again, the gyroid specimens with 5% in-fill densities could not be tested as the print density was too low to form testable specimens. The gyroid specimens had an axial shear strength of 0.33 ± 0.1 MPa for 10% in-fill, 0.97 ± 0.2 MPa for 15% in-fill, 1.76 ± 0.3 MPa for 20% in-fill, 1.96 ± 0.2 MPa for 25% in-fill, 2.92 ± 0.3 MPa for 30% in-fill, and 3.23 ± 0.2 MPa for 35% in-fill. Finally, triangle specimens had an axial strength of 0.67 ± 0.09 MPa for 5% in-fill, 0.75 ± 0.2 MPa for 10% in-fill, 0.64 ± 0.05 MPa for 15% in-fill, 0.62 ± 0.2 MPa for 20% in-fill, 1.43 ± 0.2 MPa for 25% in-fill, 1.90 ± 0.3 MPa for 30% in-fill, and 1.87 ± 0.2 MPa for 35% in-fill (Figure 9). Again, all three lattice structures were compared for statistical differences at each in-fill density and all were found to be statistically different ($p < 0.01$).

Coronal Compressive Strength for Gyroid
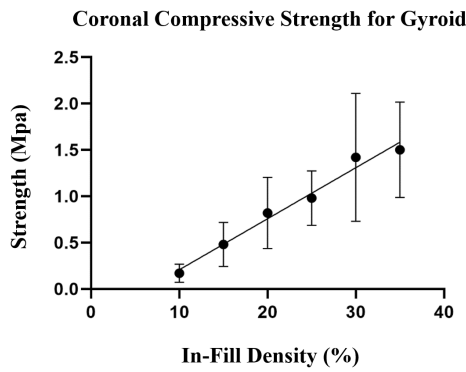
FIGURE 8 Coronal compressive strength of gyroid specimens calculated based on ultimate force at failure and cross-sectional area.

Shear Strength

FIGURE 9 Average shear strength for each specimen calculated based on ultimate load at failure and cross-sectional area. Each lattice structure was significantly different at the specific in-fill densities ($p < 0.01$).

As previously identified for structural similarity, gyroid specimens were tested in the coronal plane, as well. These specimens had a coronal shear strength of 0.4 ± 0.04 MPa for 10% in-fill, 0.9 ± 0.1 MPa for 15% in-fill, 1.2 ± 0.1 MPa for 20% in-fill, 1.9 ± 0.1 MPa for 25% in-fill, 2.6 ± 0.2 MPa for 30% in-fill, and 3.0 ± 0.3 MPa for 35% in-fill.

3.4 | Modulus of elasticity

The modulus of elasticity was calculated for each specimen from the load versus displacement curves under axial loading. Stress and strain were calculated for all time points and plotted against each other. The modulus of elasticity was calculated for each specimen and averaged based on in-fill lattice structure and density. Despite the gyroid specimens having the highest axial compressive strength, the modulus of elasticity was the lowest for this design, between 30 and 140 MPa, while the triangle designs had the highest, ranging from 150 to 350 MPa (Figure 10). The coronal modulus of elasticity of the gyroid

FIGURE 10 Average modulus of elasticity for each specimen based on calculated stress and strain at all time points throughout testing. All lattice structures were significantly different at each in-fill density ($p < 0.01$).

specimens ranged from 15.2 to 229.6 MPa. All lattice structures were significantly different at each in-fill density ($p < 0.01$).
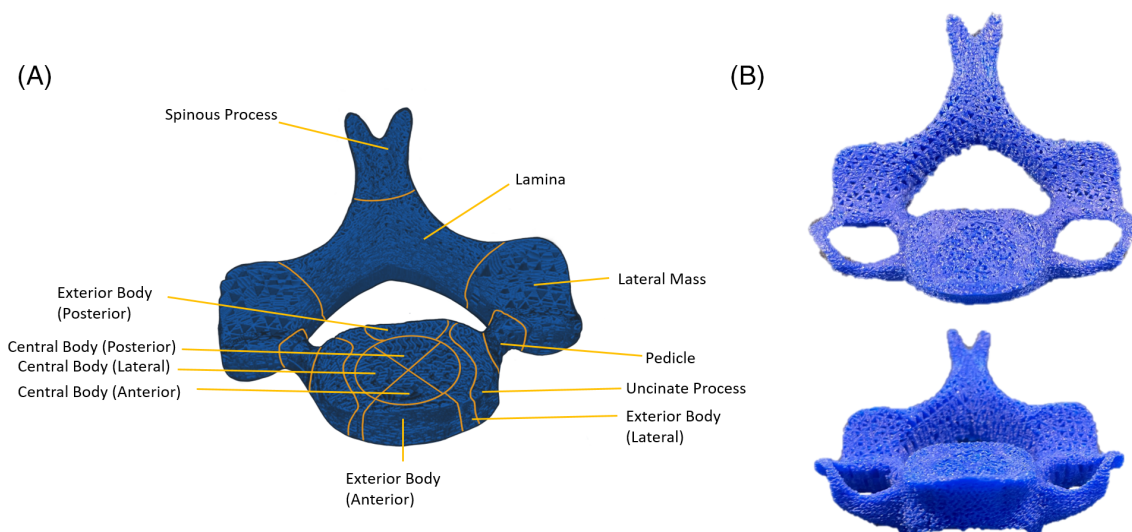
3.5 | Model creation

Following the mathematical relationships and comparison to the calculated strength values, a final 3D-printed model was constructed based on 11 specific anatomical locations of interest and the material properties calculated above (Figure 11). Specimens in this study were selected for each location based on the compressive strength of the bone at the specific anatomical location (Table 3). The model was created using a C5 cervical vertebral body in nTopology software with the exact material properties, lattice structures, and in-fill densities used in the present study. This computer model formed the final architectural framework to be able to use the results from the strength testing and create completely customizable models, with varying strengths in these eleven distinct locations, calculated from Lang et al.

Finally, one model, using the strength values of a normal cervical spine (Table 2) was then printed using the same melting temperature and print speed to ensure a seamless non-homogeneous model of the cancellous bone in the cervical spine (Figure 11).

4 | DISCUSSION

In this study, we introduced a framework for using additive manufacturing to create a tunable, customizable biomimetic model of any given cervical vertebral body. Ranges of compressive and shear strength for the cervical spine were precisely replicated using 3D printer technology. Significant differences were measured among strengths of specimens with different in-fill densities and lattice structures, as expected. Using this range, the appropriate lattice structure and density for a given strength could be selected for each of the unique 11 cervical vertebral regions. When combined, the 11 specific

FIGURE 11 (A) Final model created with altering in-fill densities, with each section assigned specifically to in-fill densities extrapolated from calculated strengths and the best-fit relationships. (B) Final 3D-printed models with 11 altering in-fill densities printed together.

TABLE 3 Compressive strengths used in the final model.

Region	Strength (MPa) via Lang et al.	Chosen structure + density	Strength (MPa) via Wahbeh et al.
Pedicle	59	Gyroid 100	60.6
Lamina	43	Gyroid 80	38.3
Lateral mass	43	Gyroid 80	38.3
Exterior body	27	Gyroid 70	26.3
Spinous process	23	Gyroid 60	20.7
Exterior body (posterior)	21	Gyroid 60	20.7
Uncinate process	21	Gyroid 60	20.7
Exterior body (anterior)	16	Gyroid 50	15.5
Central body (lateral)	15	Gyroid 50	15.5
Central body (posterior)	14	Gyroid 40	11.7
Central body (anterior)	9	Gyroid 35	9.5

regions could be defined to create a vertebra. It is important to recognize that the current model mimics that of a healthy, intact cervical spine. This specific model may not be appropriate when comparing treatments for patients with osteoporotic bone. However, due to the nature of AM, it may be possible to personalize this model for a specific patient's bone pathology, such as osteoporosis ranging from very serious to more moderate.

Unfortunately, there is a paucity of in vitro biomechanical studies assessing the material and structural properties of the cervical spine. In contrast, numerous studies have assessed these properties in other human cadaveric bones.[47,57–62] Many of these studies report on long bones. Furthermore, some authors have recently studied the lumbar spine for material and structural properties.[45,47,63] Although this provides valuable knowledge to identify a range of material strength values that a biofidelic model should fall into, the architecture of the cervical spine differs significantly to that of long bones and even the lumbar spine.[50,64,65] Specifically, the cervical spine is considerably

more porous and anisotropic than cancellous bone in other bones, making the selection of materials for a biofidelic model more challenging and, at the same time, more critical.[66]

Furthermore, material properties of cervical spine differ heavily in various locations in the cervical vertebral body itself.[51,67,68] This adds to the complexity of making an accurate biomechanical model for in vitro testing. Previous literature using CT scans was used in this study to identify different anatomical locations, and various material properties of each location were calculated using information obtained from these scans.[51] These values further show the incredibly complex architecture of the cervical vertebral body and emphasize the importance of future studies elaborating on these values and obtaining a range of strengths in the vertebral body. To our knowledge, no previous studies have biomechanically evaluated the compressive and shear strength in two different planes of various cervical cancellous locations for comparison. Despite this, the model in this study utilized values from CT scan calculations and various other

cadaveric specimens to create a model that may be similar to that of the cervical spine. With the emergence of more data on the properties at specific anatomical locations, these values can be altered and the tunability of this model becomes increasingly advantageous to potential future applications and use by independent parties.

This study identified the gyroid lattice structure as the most similar to cancellous bone, due to the final relationship between density and compressive strength, the failure modes, and the calculated strength values. Perhaps of most importance is the similarity of the relationship between the gyroid in-fill density and resultant compressive strengths. The gyroid structure was the only one to produce an exponential relationship, mimicking the widely accepted relationships between cancellous bone compressive strength and apparent density.[55] This further supports the gyroid structure being an adequate replacement for cancellous bone.

Furthermore, the failure mechanisms seen in the gyroid specimens were most similar to that of cadaveric bone. In compression, the gyroid specimens had a considerable amount of height loss, whereas the zig-zag and triangle specimens buckled at failure. In shear testing, the gyroid maintained a small amount of structural stability and was visibly twisted following failure with some cracks, whereas the zig-zag and triangle specimens split at the print line. These findings are consistent with previous AM studies that have confirmed the feasibility of creating a lattice structure similar to the composition of cancellous bone.[69] Not only is this failure pattern more similar to that of cadaveric bone, but it also represents a higher level of printing precision. Furthermore, the gyroid specimen, with PLA material, matches the majority of the cervical spine compressive strengths identified in the literature. The range of compressive strengths of the gyroid specimen were between 1.5 and 9.5 MPa and a shear strength of 0.3 and 3.2 MPa. Comparatively, the strength values of cancellous bone in literature were identified in the range of 5.1–6 MPa and a shear strength of 0.5–1.5 MPa.[48–50] The triangle and zig-zag specimens would require a very low in-fill density to replicate these features, which may compromise some of the structural properties.

Previous literature has identified gyroid lattices as a mechanically stable structure for lattice-based implants. This structure is favorable due to a high surface area to volume ratio, smooth transitions between unit cells, high toughness, and its ability to withstand stress.[70,71] Furthermore, the gyroid structure awards the highest level of microporosity and can be altered based on the desired strengths.[72] Therefore, gyroid was selected for the overall porosity and was expected to be the least strong, but perform similar to cancellous bone. As expected, the gyroid produced failure patterns similar to cancellous bone and lower strengths.

In contrast, diamond structures have been identified as a possible structure for producing anisotropy in metal implants and further being a suitable structure for implants as the porous structure mimics that of cancellous bone, promoting bony ingrowth.[73,74] For the present purposes, the similarity to cancellous bone is of the most importance. Both the triangle and zig-zag designs are based of the diamond-like structure. However, the triangles provide higher structural stability, while the zig-zag pattern is less uniform, which may better mirror the natural pattern of cancellous bone. As expected, in this study, both the triangle and zig-zag were found to be significantly stronger than the gyroid structure. However, for the purposes of replicating cancellous cervical spine, this may not be an advantageous feature. Therefore, the triangle structure was only selected for areas of high strength in the final model.

Currently, no composite models have been validated for biomechanical testing of the cervical spine. Additive manufacturing techniques, such as 3D-printing, have been used to create surgical planning and training models of the cervical spine, but have not yet been validated for biomechanical testing.[75–77] Furthermore, these techniques have begun to surface in the creation of an additively manufactured lumbar in vitro model.[33,78,79] Moreover, current commercially available models of the thoracic and lumbar spine are composed of a rigid epoxy resin and polyurethane foam creating a homogenous, isotropic model and biomechanical testing of the vertebral bone itself would not yield similar results to cancellous cervical bone, as this material does not represent cancellous bone strength in the cervical spine.[31,80–82] Therefore, this composite model is typically used for kinematic testing to evaluate range of motion under applied pure moments.[83,84] Such bone models have been highly effective for long bones, which rely heavily on diaphyseal cortical bone for structural strength; however, due to the difference in strengths and properties of cancellous bone and epoxy resin, these models could not be used for testing beyond range of motion such as initial fixation and migration testing.

The difficulties surrounding creation of the spine model may, in part, be due to the non-homogenous nature of the cancellous bone.[85,86] This, and the complex structure of the cancellous bone leading to a highly anisotropic cancellous core. Therefore, AM techniques and 3D printed models may be the best solution for cervical spine models, as it allows for high degrees of precision and completely customizable models. In this study, we introduced the first 3D-printed model of a cervical spine with an anisotropic, non-homogenous cancellous composition.

However, future studies are necessary to further verify the present model and improve upon the current design. The cortical shell is of utmost importance in the cervical spine. Cadaveric data on the material or structural properties of the cervical spine are scarce; however, the creation of the cortical shell is the next step in this study.[87–89] Shear properties can be improved in the current model, as well. Through AM software, lattice designs can be further modified to replicate certain properties and increase or decrease the strength in any given plane.[90–92] As the gyroid structure may be the most similar to cancellous bone, other lattice structures, with similar micro-structure to gyroid, should be tested to further fine-tune this model. Previous studies have demonstrated that lattice structures can be individually altered to change the material properties in different planes and orientations.[93–95] These methods can be applied to the present model to further fine-tune the properties. Finally, the overall structural strength of the model should be validated against cadaveric cervical spine specimen.

4.1 | Limitations

This study is not without limitations. One limitation is the lack of available material properties for cadaveric cervical bone. All data obtained in this study were correlated with previously published data. This may account for some variation in the calculated strength and reported strength of identified literature. Furthermore, little data was identified for cervical cancellous bone properties; therefore, some thoracic and lumbar data were utilized to identify a range of properties. Although the final model was created with cervical data, specifically the compressive strength data, data from the cervical spine for coronal compressive strength and shear strength should be obtained for a final validated model.

5 | CONCLUSIONS

To our knowledge, this study introduces the first framework for using additive manufacturing to create a tunable, customizable biomimetic model of a cervical vertebral body. The findings of the present study provide a foundation for the development of comprehensive preclinical testing of the fixation novel or existing designs of cervical disc replacements. One cervical vertebra model was successfully printed emulating the average strengths of a cervical vertebral body to ensure adequate printing capabilities with the non-homogeneous design and demonstrate feasibility. This model may provide a useful tool for a more comprehensive and efficient approach to the preclinical evaluation of CDRs, specifically for fixation testing.

AUTHOR CONTRIBUTIONS

Jenna M. Wahbeh: Conception; acquisition of data and analysis of data; interpretation of data; and drafting and editing the work. **Erika Hookasian**: Acquisition of data and analysis of data; editing of manuscript. **John Lama**: Acquisition of data and analysis of data; interpretation of data. **Labiba Alam**: Acquisition of data and analysis of data; interpretation of data. **Sang-Hyun Park**: Conception; acquisition of data and analysis of data; and interpretation of data. **Sophia N. Sangiorgio**: Conception; interpretation of data, and drafting and editing the work; and final approval for publication. **Edward Ebramzadeh**: Conception; interpretation of data; drafting and editing the work; and final approval for publication.

ACKNOWLEDGMENTS

CONFLICT OF INTEREST STATEMENT

ORCID

Jenna M. Wahbeh https://orcid.org/0000-0003-0101-5645

REFERENCES

1. MacDowall A, Canto Moreira N, Marques C, et al. Artificial disc replacement versus fusion in patients with cervical degenerative disc disease and radiculopathy: a randomized controlled trial with 5-year outcomes. *J Neurosurg Spine*. 2019;30(3):323-331.
2. Eck JC, Humphreys SC, Lim TH, et al. Biomechanical study on the effect of cervical spine fusion on adjacent-level intradiscal pressure and segmental motion. *Spine*. 2002;27(22):2431-2434.
3. Gornet MF, Burkus JK, Shaffrey ME, Nian H, Harrell FE Jr. Cervical disc arthroplasty with prestige LP disc versus anterior cervical discectomy and fusion: seven-year outcomes. *Int J Spine Surg*. 2016;10:24.
4. Gornet MF, Lanman TH, Burkus JK, et al. Two-level cervical disc arthroplasty versus anterior cervical discectomy and fusion: 10-year outcomes of a prospective, randomized investigational device exemption clinical trial. *J Neurosurg Spine*. 2019;21:1-11.
5. Malham GM, Parker RM, Ellis NJ, Chan PG, Varma D. Cervical artificial disc replacement with ProDisc-C: clinical and radiographic outcomes with long-term follow-up. *J Clin Neurosci*. 2014;21(6):949-953.
6. Wahbeh J, Bogosian C, Kistler N, Park S-H, Ebramzadeh E, Sangiorgio S. Combining all available clinical outcomes on cervical disc arthroplasty: a systematic review and meta-analysis. Journal of orthopedics and orthopedic. *Surgery*. 2022;3:1-16.
7. Shin JJ, Kim K-R, Son DW, et al. Cervical disc arthroplasty: what we know in 2020 and a literature review. *J Orthop Surg*. 2021;29(1_suppl):23094990211006934.
8. Kim KR, Chin DK, Kim KS, et al. Revision surgery for a failed artificial disc. *Yonsei Med J*. 2021;62(3):240-248.
9. Goffin J, Casey A, Kehr P, et al. Preliminary clinical experience with the Bryan cervical disc prosthesis. *Neurosurgery*. 2002;51(3):840-845. discussion 5–7.
10. Nunley PD, Cavanaugh DA, Kerr EJ 3rd, et al. Heterotopic ossification after cervical total disc replacement at 7 years-prevalence, progression, clinical implications, and risk factors. *Int J Spine Surg*. 2018;12(3):352-361.
11. Virk S, Phillips F, Khan S, Qureshi S. A cross-sectional analysis of 1347 complications for cervical disc replacements from medical device reports maintained by the United States Food and Drug Administration. *Spine J*. 2021;21(2):265-272.
12. Cao JM, Zhang YZ, Shen Y, Ding WY. Complications of Bryan cervical disc replacement. *Orthopaedic Surgery*. 2010;2(2):86-93.
13. Goffin J. Complications of cervical disc arthroplasty. *Seminars in Spine Surgery*. 2006;18:87-98.
14. Shi S, Zheng S, Li XF, Yang LL, Liu ZD, Yuan W. Comparison of 2 zero-profile implants in the treatment of single-level cervical spondylotic myelopathy: a preliminary clinical study of cervical disc arthroplasty versus fusion. *PloS One*. 2016;11(7):e0159761.
15. Mehren C, Heider F, Siepe CJ, et al. Clinical and radiological outcome at 10 years of follow-up after total cervical disc replacement. *Eur Spine J*. 2017;26(9):2441-2449.
16. Yang X, Janssen T, Arts MP, Peul WC, Vleggeert-Lankamp CLA. Radiological follow-up after implanting cervical disc prosthesis in anterior discectomy: a systematic review. *Spine J*. 2018;18(9):1678-1693.
17. Wu TK, Liu H, Wang BY, Meng Y. Minimum four-year subsequent surgery rates of cervical disc replacement versus fusion: a meta-analysis of prospective randomized clinical trials. *Orthop Traumatol Surg Res*. 2017;103(1):45-51.
18. Park JB, Chang H, Yeom JS, Suk KS, Lee DH, Lee JC. Revision surgeries following artificial disc replacement of cervical spine. *Acta Orthop Traumatol Turc*. 2016;50(6):610-618.
19. Wilke HJ, Wenger K, Claes L. Testing criteria for spinal implants: recommendations for the standardization of in vitro stability testing of spinal implants. *Eur Spine J*. 1998;7(2):148-154.
20. Patwardhan AG, Tzermiadianos MN, Tsitsopoulos PP, et al. Primary and coupled motions after cervical total disc replacement using a compressible six-degree-of-freedom prosthesis. *Eur Spine J*. 2012;21 Suppl 5(Suppl 5):S618-S629.
21. Patwardhan AG, Havey RM. Prosthesis design influences segmental contribution to total cervical motion after cervical disc arthroplasty. *Eur Spine J*. 2020;29(11):2713-2721.

22. McAfee PC, Cunningham B, Dmitriev A, et al. Cervical disc replacement—porous coated motion prosthesis: a comparative biomechanical analysis showing the key role of the posterior longitudinal ligament. *Spine*. 2003;*28*(20S):S176-S185.

23. Panjabi MM. Hybrid multidirectional test method to evaluate spinal adjacent-level effects. *Clin Biomech*. 2007;*22*(3):257-265.

24. Kienle A, Graf N, Krais C, Wilke HJ. The MOVE-C cervical artificial disc—design, materials, mechanical safety. *Med Devices (Auckl)*. 2020;*13*:315-324.

25. Sangiorgio SN, Ebramzadeh E, Longjohn DB, Dorr LD. Effects of dorsal flanges on fixation of a cemented total hip replacement femoral stem. *J Bone Joint Surg Am*. 2004;*86*(4):813-820.

26. Sangiorgio SN, Longjohn DB, Lee JL, Alexander JD, Dorr LD, Ebramzadeh E. Simulation of extreme loads on the proximal femur for implant fixation assessment. *J Appl Biomater Biomech*. 2008;*6*(2):72-80.

27. Cristofolini L, Affatato S, Erani P, Tigani D, Viceconti M. Implant fixation in knee replacement: preliminary in vitro comparison of ceramic and metal cemented femoral components. *Knee*. 2009;*16*(2):101-108.

28. Cristofolini L, Affatato S, Erani P, Leardini W, Tigani D, Viceconti M. Long-term implant—bone fixation of the femoral component in total knee replacement. *Proc Inst Mech Eng H*. 2008;*222*(3):319-331.

29. Conlisk N, Gray H, Pankaj P, Howie CR. The influence of stem length and fixation on initial femoral component stability in revision total knee replacement. *Bone Joint Res*. 2012;*1*(11):281-288.

30. Small SR, Hensley SE, Cook PL, et al. Characterization of femoral component initial stability and cortical strain in a reduced stem-length design. *J Arthroplasty*. 2017;*32*(2):601-609.

31. McKellop H, Ebramzadeh E, Niederer PG, Sarmiento A. Comparison of the stability of press-fit hip prosthesis femoral stems using a synthetic model femur. *J Orthop Res*. 1991;*9*(2):297-305.

32. Clifton W, Nottmeier E, Damon A, Dove C, Chen SG, Pichelmann M. A feasibility study for the production of three-dimensional-printed spine models using simultaneously extruded thermoplastic polymers. *Cureus*. 2019;*11*(4):e4440.

33. Bohl MA, McBryan S, Newcomb A, et al. Range of motion testing of a novel 3D-printed synthetic spine model. *Global Spine J*. 2020;*10*(4):419-424.

34. DiAngelo DJ, Foley KT, Morrow BR, et al. In vitro biomechanics of cervical disc arthroplasty with the ProDisc-C total disc implant. *Neurosurg Focus*. 2004;*17*(3):E7.

35. Lou J, Li Y, Wang B, Meng Y, Gong Q, Liu H. Biomechanical evaluation of cervical disc replacement with a novel prosthesis based on the physiological curvature of endplate. *J Orthop Surg Res*. 2018;*13*(1):41.

36. Cristofolini L, Erani P, Savigni P, Grupp T, Thies O, Viceconti M. Increased long-term failure risk associated with excessively thin cement mantle in cemented hip arthroplasty: a comparative in vitro study. *Clin Biomech (Bristol, Avon)*. 2007;*22*(4):410-421.

37. Engh CA, O'connor D, Jasty M, McGovern TF, Bobyn JD, Harris WH. Quantification of implant micromotion, strain shielding, and bone resorption with porous-coated anatomic medullary locking femoral prostheses. *Clin Orthop Relat Res*. 1992;*285*:13-29.

38. Wei F, Li Z, Liu Z, et al. Upper cervical spine reconstruction using customized 3D-printed vertebral body in 9 patients with primary tumors involving C2. *Ann Transl Med*. 2020;*8*(6):332.

39. Xu N, Wei F, Liu X, et al. Reconstruction of the upper cervical spine using a personalized 3D-printed vertebral body in an adolescent with Ewing sarcoma. *Spine*. 2016;*41*(1):E50-E54.

40. Clifton W, Damon A, Valero-Moreno F, Nottmeier E, Pichelmann M. The SpineBox: a freely available, open-access, 3D-printed simulator design for lumbar pedicle screw placement. *Cureus*. 2020;*12*(4):e7738.

41. Clifton W, Nottmeier E, Damon A, Dove C, Pichelmann M. The future of biomechanical spine research: conception and design of a dynamic 3D printed cervical myelography phantom. *Cureus*. 2019;*11*(5):e4591.

42. Gibson LJ. Cellular solids. *MRS Bulletin*. 2003;*28*(4):270-274.

43. Gibson LJ. Modelling the mechanical behavior of cellular materials. *Mater Sci Eng A*. 1989;*110*:1-36.

44. Naboni R, Kunic A. *Design and additive manufacturing of lattice-based cellular solids at building scale*; XXI Congreso Internacional de la Sociedad Iberoamericana de Gráfica Digital, Blucher Design Proceedings; 2017:369-375.

45. Wang F, Metzner F, Zheng L, Osterhoff G, Schleifenbaum S. Selected mechanical properties of human cancellous bone subjected to different treatments: short-term immersion in physiological saline and acetone treatment with subsequent immersion in physiological saline. *J Orthop Surg Res*. 2022;*17*(1):376.

46. Ogurkowska MB, Błaszczyk A. Distribution of Young's modulus at various sampling points in a human lumbar spine vertebral body. *Spine J*. 2020;*20*:1861-1875.

47. Nicholson PH, Cheng XG, Lowet G, et al. Structural and material mechanical properties of human vertebral cancellous bone. *Med Eng Phys*. 1997;*19*(8):729-737.

48. Xavier F, Jauregui JJ, Cornish N, et al. Regional variations in shear strength and density of the human thoracic vertebral endplate and trabecular bone. *Int J Spine Surg*. 2017;*11*(1):7.

49. Feng H, Ma Y, Wang SJ, Zhang S, Li Z. The correlation of regional microstructure and mechanics of the cervical articular process in adults. *Materials (Basel)*. 2021;*14*(21):6409.

50. Shim VPW, Yang LM, Liu JF, Lee VS. Characterisation of the dynamic compressive mechanical properties of cancellous bone from the human cervical spine. *Int J Impact Eng*. 2005;*32*(1):525-540.

51. Anderst WJ, Thorhauer ED, Lee JY, Donaldson WF, Kang JD. Cervical spine bone mineral density as a function of vertebral level and anatomic location. *Spine J*. 2011;*11*(7):659-667.

52. Lang SM, Moyle DD, Berg EW, et al. Correlation of mechanical properties of vertebral trabecular bone with equivalent mineral density as measured by computed tomography. *J Bone Joint Surg Am*. 1988;*70*(10):1531-1538.

53. McBroom RJ, Hayes WC, Edwards WT, Goldberg RP, White AA 3rd. Prediction of vertebral body compressive fracture using quantitative computed tomography. *J Bone Joint Surg Am*. 1985;*67*(8):1206-1214.

54. Fleps I, Bahaloo H, Zysset PK, Ferguson SJ, Pálsson H, Helgason B. Empirical relationships between bone density and ultimate strength: a literature review. *J Mech Behav Biomed Mater*. 2020;*110*:103866.

55. Carter DR, Hayes WC. Bone compressive strength: the influence of density and strain rate. *Science*. 1976;*194*(4270):1174-1176.

56. Fyhrie DP, Schaffler MB. Failure mechanisms in human vertebral cancellous bone. *Bone*. 1994;*15*(1):105-109.

57. Li B, Aspden RM. Composition and mechanical properties of cancellous bone from the femoral head of patients with osteoporosis or osteoarthritis. *J Bone Miner Res*. 1997;*12*(4):641-651.

58. Goldstein SA. The mechanical properties of trabecular bone: dependence on anatomic location and function. *J Biomech*. 1987;*20*(11–12):1055-1061.

59. Morgan EF, Unnikrisnan GU, Hussein AI. Bone mechanical properties in healthy and diseased states. *Annu Rev Biomed Eng*. 2018;*4*(20):119-143.

60. Oftadeh R, Perez-Viloria M, Villa-Camacho JC, Vaziri A, Nazarian A. Biomechanics and mechanobiology of trabecular bone: a review. *J Biomech Eng*. 2015;*137*(1):0108021-01080215.

61. Schoenfeld CM, Lautenschlager EP, Meyer PR. Mechanical properties of human cancellous bone in the femoral head. *Med Biol Eng*. 1974;*12*(3):313-317.

62. Evans FG. *Mechanical properties of bone*. Vol 1973. Charles C. Thomas; 1973:241-243.

63. Zehra U, Robson-Brown K, Adams MA, Dolan P. Porosity and thickness of the vertebral endplate depend on local mechanical loading. *Spine*. 2015;*40*(15):1173-1180.

64. Kopperdahl DL, Roberts AD, Keaveny TM. Localized damage in vertebral bone is most detrimental in regions of high strain energy density. *J Biomech Eng*. 1999;*121*(6):622-628.

65. Bland JH, Boushey DR. Anatomy and physiology of the cervical spine. *Semin Arthritis Rheum*. 1990;*20*:1-20.

66. Vedantam A, Eckardt G, Wang MC, Schmit BD, Kurpad SN. Clinical correlates of high cervical fractional anisotropy in acute cervical spinal cord injury. *World Neurosurg*. 2015;*83*:824-828.

67. Keller TS, Hansson TH, Abram AC, Spengler DM, Panjabi MM. Regional variations in the compressive properties of lumbar vertebral trabeculae. Effects of disc degeneration. *Spine*. 1989;*14*(9):1012-1019.

68. Amstutz HC, Sissons HA. The structure of the vertebral spongiosa. *J Bone Joint Surg Br*. 1969;*51*(3):540-550.

69. McGregor M, Patel S, McLachlin S, Mihaela V. Architectural bone parameters and the relationship to titanium lattice design for powder bed fusion additive manufacturing. *Addit Manuf*. 2021;*47*:102273.

70. Al-Ketan O, Lee D-W, Rowshan R, Abu Al-Rub RK. Functionally graded and multi-morphology sheet TPMS lattices: design, manufacturing, and mechanical properties. *J Mech Behav Biomed Mater*. 2020;*102*:103520.

71. Timercan A, Sheremetyev V, Brailovski V. Mechanical properties and fluid permeability of gyroid and diamond lattice structures for intervertebral devices: functional requirements and comparative analysis. *Sci Technol Adv Mater*. 2021;*22*(1):285-300.

72. du Plessis A, Razavi SMJ, Berto F. The effects of microporosity in struts of gyroid lattice structures produced by laser powder bed fusion. *Mater Des*. 2020;*194*:108899.

73. Wauthle R, Vrancken B, Beynaerts B, et al. Effects of build orientation and heat treatment on the microstructure and mechanical properties of selective laser melted Ti6Al4V lattice structures. *Addit Manuf*. 2015;*5*:77-84.

74. Liu F, Zhang DZ, Zhang P, Zhao M, Jafar S. Mechanical properties of optimized diamond lattice structure for bone scaffolds fabricated via selective laser melting. *Materials*. 2018;*11*(3):374.

75. Wilcox B, Mobbs RJ, Wu AM, Phan K. Systematic review of 3D printing in spinal surgery: the current state of play. *J Spine Surg*. 2017;*3*(3):433-443.

76. Samdani UF, Hwang SW. 3D printing in spine surgery: current and future applications. *J 3D Print Med*. 2021;*5*(3):145-153.

77. Syed M, Neavling N, Mariotti BL, et al. Materials review: 3D printing a biomechanically accurate cervical spine model for surgical education and case preparation. *J 3D Print Med*. 2022;*6*(2):95-103.

78. Bohl MA, Mooney MA, Repp GJ, et al. The Barrow biomimetic spine: fluoroscopic analysis of a synthetic spine model made of variable 3D-printed materials and print parameters. *Spine*. 2018;*43*(23):E1368-E1375.

79. Bohl MA, Morgan CD, Mooney MA, et al. Biomechanical testing of a 3D-printed L5 vertebral body model. *Cureus*. 2019;*11*(1):e3893.

80. Heiner AD, Brown TD. Structural properties of a new design of composite replicate femurs and tibias. *J Biomech*. 2001;*34*(6):773-781.

81. Crowninshield RD, Pedersen DR, Brand RA. A measurement of proximal femur strain with total hip arthroplasty. *J Biomech Eng*. 1980;*102*(3):230-233.

82. Cristofolini L, Viceconti M, Cappello A, Toni A. Mechanical validation of whole bone composite femur models. *J Biomech*. 1996;*29*(4):525-535.

83. Wheeler DJ, Freeman AL, Ellingson AM, et al. Inter-laboratory variability in in vitro spinal segment flexibility testing. *J Biomech*. 2011;*44*(13):2383-2387.

84. Sherrill JT, Siddicky SF, Davis WD, Chen C, Bumpass DB, Mannen EM. Validation of a custom spine biomechanics simulator: a case for standardization. *J Biomech*. 2020;*98*:109470.

85. Smit TH, Odgaard A, Schneider E. Structure and function of vertebral trabecular bone. *Spine*. 1997;*22*(24):2823-2833.

86. Schröder G, Jabke B, Schulze M, et al. A comparison, using X-ray micro-computed tomography, of the architecture of cancellous bone from the cervical, thoracic and lumbar spine using 240 vertebral bodies from 10 body donors. *Anat Cell Biol*. 2021;*54*(1):25-34.

87. Ritzel H, Amling M, Pösl M, Hahn M, Delling G. The thickness of human vertebral cortical bone and its changes in aging and osteoporosis: a Histomorphometric analysis of the complete spinal column from thirty-seven autopsy specimens. *J Bone Miner Res*. 1997;*12*(1):89-95.

88. Scheinpflug J, Pfeiffenberger M, Damerau A, et al. Journey into bone models: a review. *Genes (Basel)*. 2018;*9*(5):247.

89. Karaikovic EE, Daubs MD, Madsen RW, Gaines RWJ. Morphologic characteristics of human cervical pedicles. *Spine*. 1997;*22*(5):493-500.

90. Fernandes RR, Tamijani AY. Design optimization of lattice structures with stress constraints. *Mater Des*. 2021;*210*:110026.

91. Kang D, Park S, Son Y, Yeon S, Kim SH, Kim I. Multi-lattice inner structures for high-strength and light-weight in metal selective laser melting process. *Mater Des*. 2019;*175*:107786.

92. Richard CT, Kwok TH. Analysis and design of lattice structures for rapid-investment casting. *Materials (Basel)*. 2021;*14*(17):4867.

93. Harrison N, McHugh PE, Curtin W, Mc DP. Micromotion and friction evaluation of a novel surface architecture for improved primary fixation of cementless orthopaedic implants. *J Mech Behav Biomed Mater*. 2013;*21*:37-46.

94. Hossain U, Ghouse S, Nai K, Jeffers JRT. Mechanical and morphological properties of additively manufactured SS316L and Ti6Al4V microstruts as a function of build angle. *Addit Manuf*. 2021;*46*:102050.

95. Pobloth AM, Checa S, Razi H, et al. Mechanobiologically optimized 3D titanium-mesh scaffolds enhance bone regeneration in critical segmental defects in sheep. *Sci Transl Med*. 2018;*10*(423):eaam8828.